nature communications

Article

https://doi.org/10.1038/s41467-022-34884-4

Discovery of $LaAlO_3$ as an efficient catalyst for two-electron water electrolysis towards hydrogen peroxide

Received: 1 March 2022

Accepted: 4 November 2022

Published online: 25 November 2022

Check for updates

Jihyun Baek[1,5], Qiu Jin[2,5], Nathan Scott Johnson[3], Yue Jiang[1], Rui Ning[4], Apurva Mehta[3], Samira Siahrostami[2] ✉ & Xiaolin Zheng[1] ✉

Electrochemical two-electron water oxidation reaction (2e-WOR) has drawn significant attention as a promising process to achieve the continuous on-site production of hydrogen peroxide (H_2O_2). However, compared to the cathodic H_2O_2 generation, the anodic 2e-WOR is more challenging to establish catalysts due to the severe oxidizing environment. In this study, we combine density functional theory (DFT) calculations with experiments to discover a stable and efficient perovskite catalyst for the anodic 2e-WOR. Our theoretical screening efforts identify $LaAlO_3$ perovskite as a stable, active, and selective candidate for catalyzing 2e-WOR. Our experimental results verify that $LaAlO_3$ achieves an overpotential of 510 mV at 10 mA cm^{-2} in 4 M K_2CO_3/$KHCO_3$, lower than those of many reported metal oxide catalysts. In addition, $LaAlO_3$ maintains a stable H_2O_2 Faradaic efficiency with only a 3% decrease after 3 h at 2.7 V vs. RHE. This computation-experiment synergistic approach introduces another effective direction to discover promising catalysts for the harsh anodic 2e-WOR towards H_2O_2.

Hydrogen peroxide (H_2O_2) is an environmentally benign and powerful chemical oxidizer widely used in electronics manufacturing[1,2], chemical synthesis[3,4], water purification[5], and many other industrial sectors. Currently, H_2O_2 is produced by the anthraquinone process, which necessitates an energy-demanding multi-electron process and massive infrastructures to transport it to the point of use[6]. Recently, electrochemical processes, such as two-electron oxygen reduction reaction (2e-ORR) and water oxidation reaction (2e-WOR)[7–9], have emerged as attractive routes to produce H_2O_2 onsite in small-scale distributed units[10]. The 2e-ORR has been extensively investigated, and many suitable catalysts with high activity and selectivity have been reported, including noble metals[10–12], carbon materials[13,14], and transition metals[15,16]. Unlike 2e-ORR which needs oxygen, the 2e-WOR only requires water as a reactant, thus simplifying the system for the synthesis of H_2O_2. The pioneering research on H_2O_2 production via 2e-WOR in 2004 showed the feasibility of this process using a carbon-based catalyst in the alkaline electrolyte[17]. Most recent reports on the 2e-WOR catalysts have focused on using metal oxides[18–24], doped metal oxides[25,26], heterostructure[27,28], carbon-based materials[29–31], and electrolyte engineering[32,33]. However, the 2e-WOR still needs significant improvement in electrocatalysts to be more stable, active, and selective.

The elementary steps for the 2e-WOR are associated with the interaction between the catalyst surface and oxygen intermediates: *O, *OH, and *OOH[34]. For a catalyst to be selective for the 2e-WOR, the binding energy of those intermediates should be in the right range. If the binding is too strong, the adsorbed OH* is further oxidized to *O and *OOH, facilitating 4e-WOR for O_2 evolution. If the binding is too weak, it is difficult to activate the water molecule and form the *OH. Currently, for 2e-WOR, the state-of-the-art metal oxide catalysts still

[1]Department of Mechanical Engineering, Stanford University, Stanford, CA 94305, USA. [2]Department of Chemistry, University of Calgary, Calgary, AB T2N 1N4, Canada. [3]Stanford Synchrotron Radiation Lightsource, SLAC National Accelerator Laboratory, Menlo Park, CA 94025, USA. [4]Department of Materials Science and Engineering, Stanford University, Stanford, CA 94305, USA. [5]These authors contributed equally: Jihyun Baek, Qiu Jin.
✉e-mail: samira.siahrostami@ucalgary.ca; xlzheng@stanford.edu

show more than 1 V overpotential from the equilibrium potential for H_2O_2 (1.76 V vs. RHE) to reach 10 mA cm^{-2} of the current density[18,19,21,25].

Recently, perovskite oxides have garnered significant attention in numerous applications, such as electronics[35], energy conversion and storage[36], and catalysts[37,38]. Perovskites have a unit formula ABO_3, where A cation sites are usually rare-earth or alkaline earth metal, and B cations are typically small transition metal elements staying at the centre of the oxygen octahedron[39]. Perovskites incorporate a broad combination of A and B cations, using more than 90% of metallic elements in the periodic table[39]. As such, perovskites provide rich opportunities to tune their chemical, physical, and catalytic properties.

A superior catalyst for 2e-WOR must meet the following three requirements: (i) high stability to fulfil the demand for long-term operation; (ii) high selectivity to prevent the formation of by-products; (iii) high activity to save energy input. We investigated the stability through a computational screening of a vast number of perovskites in the Materials Project database[40] as suggested by Persson et al.[41] This approach has proven to be powerful in rapidly excluding a variety of catalyst materials that do not fall within the desired stability target for long term and practical application. This approach was first introduced by Persson et al. to discover synthesizable and robust photocatalysts for CO_2 reduction reactions via computational analysis[42]. The recent work by Gunasooriya and Nørskov is another example of applying this approach to discovering stable oxides for the oxygen reduction reaction[43]. Following this approach, we study an extensive library of more than 2000 perovskites to identify 32 stable perovskites at pH = 8 and 10 stable perovskites at pH = 11, conditions relevant for 2e-WOR. Among the 32 stable perovskites, $LaAlO_3$ stands out as the most stable perovskite from this study. We further study the activity and selectivity of a series of four other Lanthanum-based (La-based) perovskites including $LaCuO_3$, $LaNiO_3$ $LaGaO_3$, and $LaZnO_3$ using density functional theory (DFT) calculation and reported data in the literature[44,45]. We show that $LaAlO_3$ is not only the most stable but also the most active and selective catalyst for 2e-WOR among other stable La-based perovskites. It is also the most active, selective, and stable material reported so far[8,18,19,21,25,46]. To verify the computational prediction, we synthesize $LaAlO_3$ thin films on FTO glass using the solution-combustion method. The synthesized $LaAlO_3$ thin film is confirmed to have a cubic perovskite crystal structure with the dominant phases of (110) and (111) through transmission electron microscopy (TEM), grazing-incidence X-ray diffraction (GIXRD), and X-ray photoelectron spectroscopy (XPS) analysis. Moreover, the $LaAlO_3$ thin film has excellent catalytic properties towards 2e-WOR, with an onset potential of 510 mV at 10 mA cm^{-2}, a peak faradaic efficiency (FE) of 87% at 3.34 V vs. RHE, H_2O_2 production rates of 0.16 mmol cm^{-2} (128 ppm) and 1.23 mmol cm^{-2} (808 ppm) at 2.7 and 3.2 V vs. RHE after 3 h, and good stability over 3 h of testing, supporting the theoretical results.

Results and discussion

Computational analysis

As discussed above, stability is a major challenge for catalysts under the harsh anodic oxidation potential conditions required for 2e-WOR toward H_2O_2 production. Under highly oxidizing 2e-WOR conditions, lack of catalyst stability is a major cause of catalyst degradation, resulting in a loss of catalytic activity and selectivity[25]. Thus, we first place a particular emphasis on filtering the stable perovskites out of more than 2,000 ABO_3 structures (Fig. 1). We applied three stability criteria. First, the decomposition energy, defined as a difference between the Gibbs free energies of perovskites and the most stable product they are decomposed to in aqueous media[41], to be <0.1 eV. The selection of the 0.1 eV threshold was based on the recommendation by Persson et al. to assure the highest stability for perovskites[47]. The second criterion is to be stable under electrochemical conditions (pH = 8 and pH = 11 with applied electrode potentials of 2.23 and 2.41 V versus SHE, respectively) using Pourbaix diagram analyzer using Python Material Genome (Pymatgen)[48] and Materials Project[40]

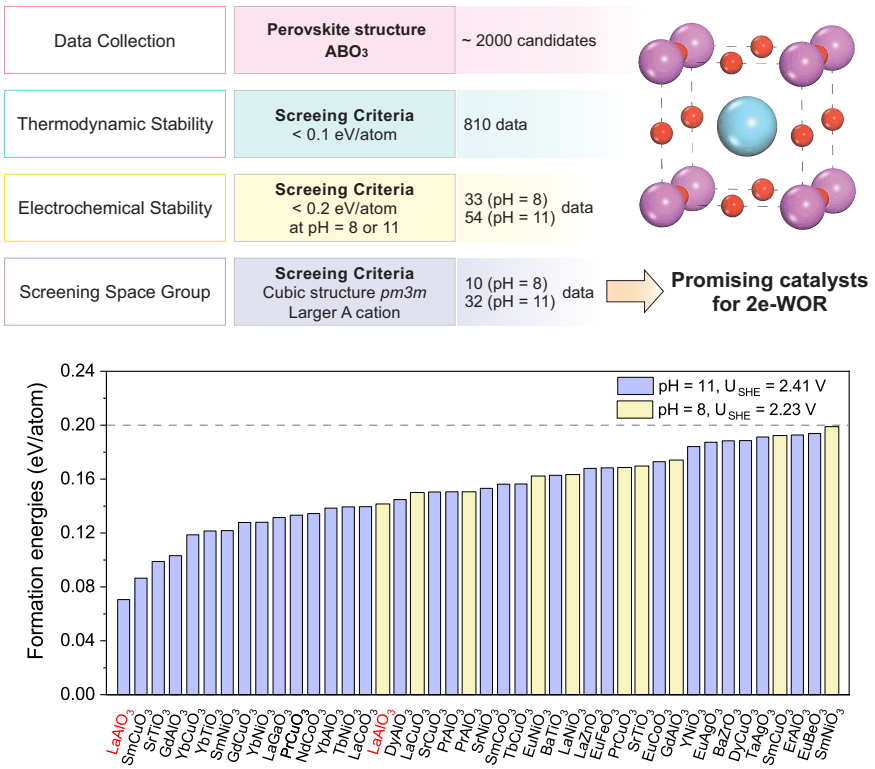

Fig. 1 | Computational screening to discover the most stable perovskite oxide under different pH conditions. Filtering stable ABO_3 perovskite structures based on three screening criteria including decomposition energy < 0.1 eV and electrochemical stability under pH = 8 and 11.

https://doi.org/10.1038/s41467-022-34884-4

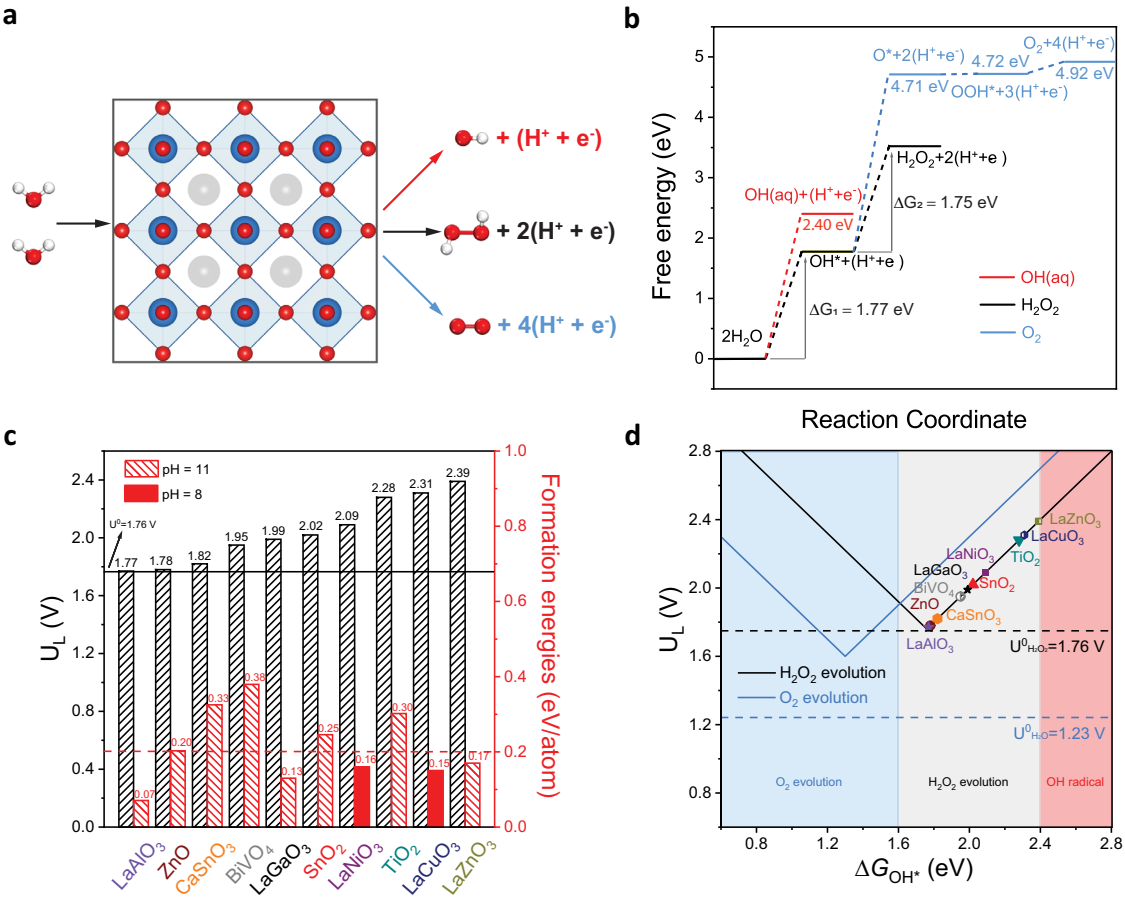

Fig. 2 | Mechanism of the 2e-WOR H_2O_2 production in $LaAlO_3$ and comparison of limiting potential and formation energy with different catalysts. a WOR processes via different pathways. La, Al, O, and H are represented by gray, blue, red, and white spheres, respectively. **b** Free energy diagram of all the three WORs over $LaAlO_3$. **c** Calculated limiting potentials (U_L, left axis) for the metal oxides, and the corresponding formation energies (right axis) under 2e-WOR (electrolyte pH = 11 or 8). **d** Volcano plots of limiting potential as a function of ΔG_{OH^*}.

cooperatively. The pH=8 and pH=11 were chosen because they are the operating conditions in most experimental studies for 2e-WOR[18,29]. The last criterion is only to include structures with cubic $Pm\bar{3}m$ space group and a larger A cation as they are the most stable and typical crystal structures for ABO_3 perovskites. The use of these three criteria yields 10 (Fig. 1 and Supplementary Table 1) and 32 (Fig. 1 and Supplementary Table 2) stable perovskites at pH = 8 and 11, respectively. Among them, $LaAlO_3$ was identified as the most stable with the least formation energy at both pH values (pH = 8 and 11). Additionally, the superior stability of $LaAlO_3$ has been revealed by the extremely high O-vacancy formation energy of 2.91 eV, as shown in Supplementary Fig. 1. The less stable perovskites with higher formation energies are more likely to suffer from catalyst aging, thereby resulting in catalyst deactivation and the demand of more frequent catalyst replacement in the device to maintain a target level of H_2O_2 production. We note that the stability analysis based on the Pourbaix diagram analyzer, introduced by Persson et al.[41] is established based on sole thermodynamic analysis with no consideration of the possible kinetic stability as a result of the slow dissolution process or formation of resistant films on the catalyst surface under reaction conditions. Previous studies show that materials such as $BiVO_4$[25] for the 2e-water oxidation reaction that does not come out as a stable material from the Pourbaix diagram analysis can survive the anodic reaction conditions for several hours. On the other hand, approaches can be taken to increase the stability of those materials. For example, doping $BiVO_4$ with Gadolinium has been used as a strategy to improve the long-term stability of $BiVO_4$ by preventing the leaching of vanadate ions[25]. In this work, we used the Pourbaix Diagram analysis to mark the materials that inherently have high stability, not taking into account the ones that may not be thermodynamically stable but may show kinetic stability as a result of a slow dissolution process under reaction conditions or those that may make a resistant film under reaction conditions. Moreover, since $LaAlO_3$ is the most stable perovskite under 2e-WOR conditions, it is highly promising to eliminate the effect of catalyst degradation, maintain catalytic performance and extend its stability to meet the long-term operation targets. Apart from the exceptional stability, $LaAlO_3$ is earth-abundant and non-toxic, providing a potential to investigate the 2e-WOR activity for $LaAlO_3$, which will be described in the later section.

Next, we employed DFT calculation to evaluate the theoretical activity and selectivity of $LaAlO_3$ for 2e-WOR. Water oxidation may follow four-electron, two-electron, and one-electron pathways (Fig. 2a); hence selectivity toward H_2O_2 product is a great challenge. Previous studies have identified that the binding energies of different reaction intermediates (O*, OH*, and OOH*) are suitable descriptors for the activity and selectivity of water oxidation reaction pathways[7,8]. An active catalyst for 2e-WOR has an optimum OH* binding ($\Delta G_{OH^*} \geq 1.76$ eV with reference to H_2O). In order to be selective, the catalyst should weakly bind O* ($\Delta G_{O^*} \geq 3.52$ eV) to suppress the 4e-WOR route and prevent the further oxidation of H_2O_2 to O_2. Moreover, the catalyst should bind OH* below 2.4 eV ($\Delta G_{OH^*} < 2.4$ eV) to avoid the formation and release of OH radicals. For $LaAlO_3$ (100) surface, the adsorption energies of these critical intermediates are $\Delta G_{OH^*} = 1.77$ eV and $\Delta G_{O^*} = 4.71$ eV (Supplementary Fig. 2). Thus, $LaAlO_3$ is highly selective

https://doi.org/10.1038/s41467-022-34884-4

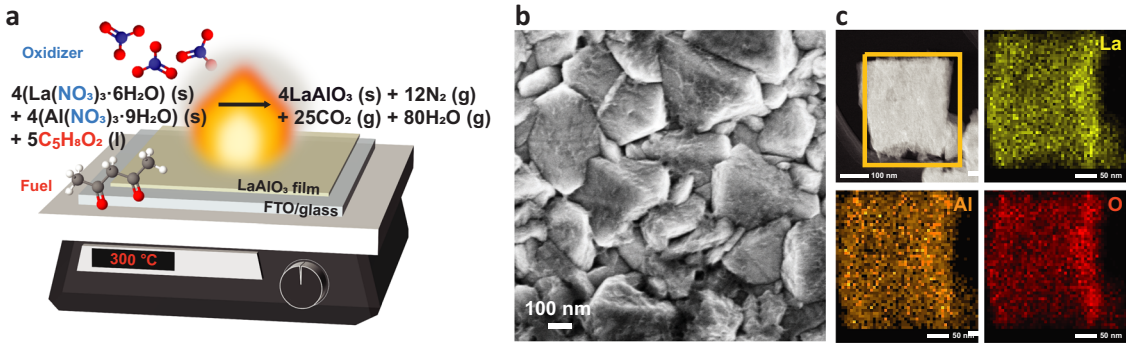

Fig. 3 | Solution combustion synthesis process and characterizations of the final product. a Schematic of low-temperature solution combustion processing mechanism for $LaAlO_3$ synthesis. **b** SEM top-view and **c** TEM dark-field and EDS mapping images of the synthesized $LaAlO_3$.

and active for the 2e-WOR and suppresses both the 1e- and the 4e-WOR pathways, as shown in Fig. 2b. Note that the (100) facet of $LaAlO_3$ was used in this analysis, as it is predicted as the most stable among (100), (110), and (111) facets based on surface energy calculations (Supplementary Fig. 3).

In addition to $LaAlO_3$, we investigated the 2e-WOR of four other La-based perovskites that were identified as stable materials in Fig. 1. We performed explicit calculations for $LaCuO_3$ and $LaNiO_3$ (Supplementary Fig. 4) and data for $LaGaO_3$ and $LaZnO_3$ were extracted from the literatures[44,45]. The calculated limiting potential (U_L) and relative stability of $LaAlO_3$ are compared in Fig. 2c to four other La-based perovskites as well as several oxides that have been evaluated for 2e-WOR[18,19]. The solid upper line marks the thermodynamic potential of 1.76 V for 2e-WOR. The lower dashed line indicates the electrochemical stability with a formation energy of 0.2 eV/atom. Figure 2c shows that $LaAlO_3$ is the most active La-based perovskite (with the lowest calculated limiting the potential of 1.77 eV) and the most stable (pH = 11, results for pH = 8 in Supplementary Fig. 5) catalyst among previously reported oxides under 2e-WOR conditions. Figure 2d shows the U_L vs. ΔG_{OH^*} for those oxides and perovskites. The binding of OH* on the $LaAlO_3$ surface is 1.77 eV which is the closest to the optimal value of 1.76 eV. In addition, we performed the Bader charge analysis to understand the active site in $LaAlO_3$ (Supplementary Fig. 6). Our results revealed a strong electron-accepting feature on the Al sites, characterized by higher charges (+2.41 to +2.43 e) as compared to the ones on La (+2.05 to +2.07 e) coming from its oxophilic nature. These more positive charges can facilitate the adsorption of negatively charged OH species in the alkaline electrolyte and thereby increase the activity of $LaAlO_3$ toward 2e-WOR. To understand the contribution of O-vacancies and defects in the activity of $LaAlO_3$, we calculated the OH* adsorption on $LaAlO_3$ with O-vacancy (Supplementary Fig. 1c). The O-vacancies are strongly binding to the OH* intermediate ($\Delta G_{OH^*} = -2.51$ eV), indicating the O-vacancies do not contribute to the 2e-WOR. Since the formation of additional O-vacancies in $LaAlO_3$ is strongly endothermic (by ~3 eV) as stated above, it is unlikely for $LaAlO_3$ to form additional defects under 2e-WOR conditions. Thus, according to the DFT results, $LaAlO_3$ is the stable, active, and selective catalyst for 2e-WOR.

We note that the carbonate anion has also been considered in the H_2O_2 reaction calculation since it is essential in the commonly used electrolyte (2 M $KHCO_3$)[18,32,49]. To evaluate the effect of carbonate anion on H_2O_2 production, we calculated the 2e-WOR pathway with carbonate anion as a mediator as reported by Fan et al. (Supplementary Fig. 7)[50]. This analysis shows that the largest free energy change via carbonate mediated pathway is 2.03 eV to generate H_2O_2, indicating that the theoretical limiting potential is 2.03 V, slightly higher than that of 2e-WOR pathway without carbonate (1.77 V). Additionally, we calculated the H_2CO_3 oxidation mechanism proposed by Kusama et al. (Supplementary Fig. 8) on the $LaAlO_3$ surface[51]. Our results agree well with the report by them and show that the first proton removal from the adsorbed H_2CO_3 is the rate-limiting step. The energy difference we calculated for this step is 1.89 eV, indicating a limiting potential of 1.89 V. This limiting potential of 1.89 V is also slightly (~0.1 V) higher than the value calculated for 2e-WOR on bare $LaAlO_3$ (1.77 V). However, all these three values (2.03, 1.77 and 1.89 V) are reasonably close, and under the operating reaction potentials all pathways will be accessible. Thus, we conclude that the carbonate and H_2CO_3 oxidation provide additional pathways to promote the H_2O_2 production.

Synthesis of $LaAlO_3$ perovskite oxide catalyst

The synthesis of $LaAlO_3$ perovskite oxide requires a high temperature of 800–1700 °C to obtain a pure cubic crystal structure with a space group of $Pm\bar{3}m$, and $LaAlO_3$ has been synthesized by methods such as the solid-state reaction of Al_2O_3 and La_2O_3[52,53], co-precipitation[54], aerosol technique[55], and sol-gel method[56,57]. To remove the need for such a high-temperature source, we employed a self-sustaining solution-based combustion synthesis method[58,59] to prepare $LaAlO_3$ that requires heating only at 300 °C. As illustrated in Fig. 3a, acetylacetone ($C_5H_8O_2$) and metal nitrates serve as fuel and oxidizers, and their reaction onset temperature is about 240 °C as determined by the thermogravimetric analysis (TGA) and differential scanning calorimeter (DSC) measurement (Supplementary Fig. 9). The mixture of metal nitrates and acetylacetone was spin-coated on an FTO glass, and we set the hot plate at 300 °C to have sufficient temperature to initiate their exothermic reaction, and the generated heat enabled the conversion of the metal precursors to $LaAlO_3$ and other gaseous products. The synthesis conditions, in terms of the precursor ratio, processing temperature, and the number of coating layers on the activity, are summarized in Supplementary Fig. 10. Fig. 3b shows the top-view scanning electron microscopy (SEM) image of as-synthesized $LaAlO_3$ on the FTO glass. The bare FTO has grains of several hundred nanometers scale with smooth surfaces. After the $LaAlO_3$ film is deposited on top, the FTO glass looks similar, but the grain surface looks rougher and more wrinkled, which looks like 2D sheets with a thickness of roughly 20–30 nm (Supplementary Fig. 11). The transmission electron microscopy (TEM) dark-field image and energy-dispersive X-ray spectroscopy (EDS) elemental analysis in Fig. 3c and SEM-EDS mapping images on several spots throughout the film in Supplementary Fig. 11 show that all elements (La, Al, and O) are uniformly distributed throughout the whole area of the film.

Material characterizations of $LaAlO_3$ perovskite

High-resolution TEM (HRTEM) images of $LaAlO_3$ in Fig. 4a reveal that the particles are composed of both amorphous and crystalline parts (yellow circles). As shown in Fig. 4b, c, and Supplementary Fig. 12, HRTEM images show that the cubic structure with a space group of $Pm\bar{3}m$ of the $LaAlO_3$ phase belongs to the (100) and (110) planes, which has a lattice spacing of 3.8 and 2.7 Å, respectively. Moreover, these planes in $Pm\bar{3}m$ space group have formation energies of 0.11 and

https://doi.org/10.1038/s41467-022-34884-4

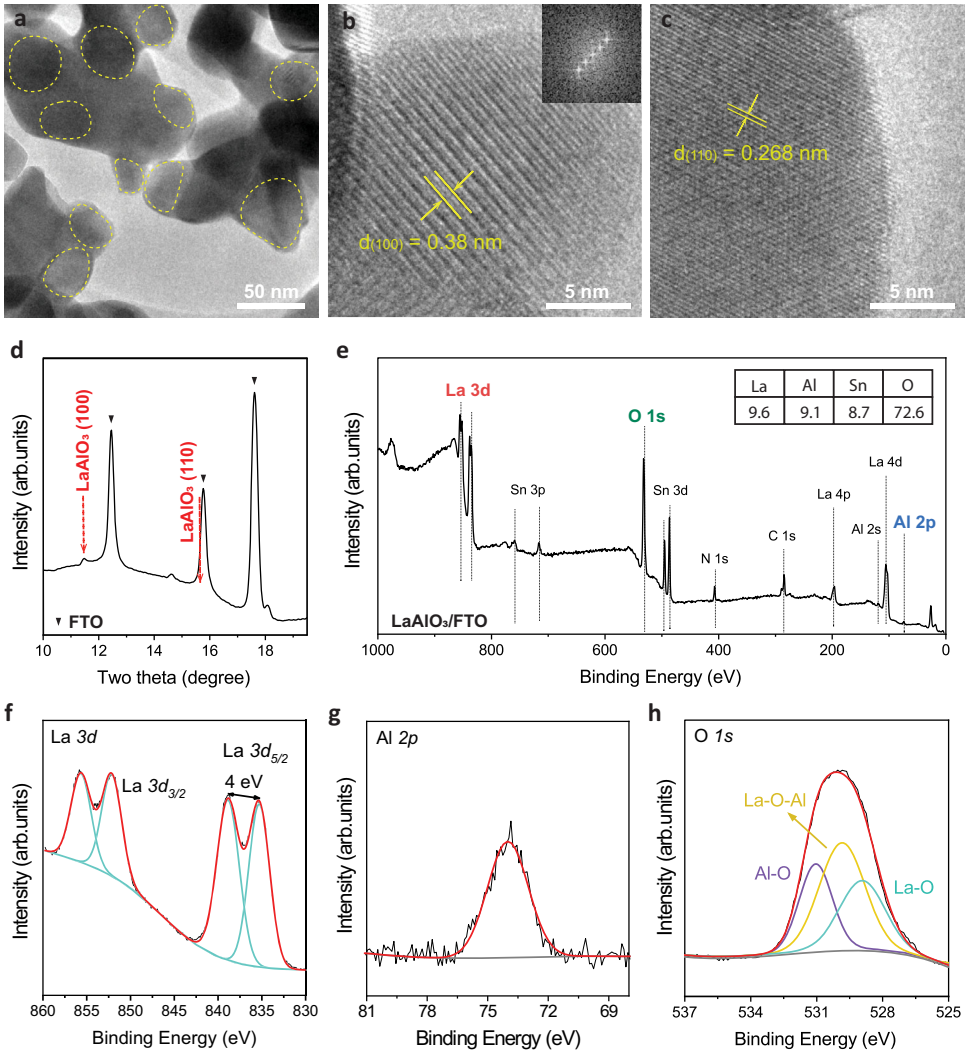

Fig. 4 | Key characterizations of the synthesized $LaAlO_3$. a–c High-resolution TEM images of $LaAlO_3$ synthesized by sol-gel combustion method. From the TEM images, the morphology shows an irregular shape with the size of several tens of nm. And most of the parts look amorphous, while a crystalline $LaAlO_3$ phase was created at some surface parts. This resulted from the temperature spontaneously attained during the combustion process instantaneously that extends to the range of 2000 °C for short periods. **d** GIXRD result of $LaAlO_3$ on FTO/glass substrate, **e** Surface analysis using XPS survey spectra with the inlet table with the elemental concentration (%), and the detailed elemental regions: **f** La 3d, **g** Al 2p, and **h** O 1 s.

0.28 eV/atom, which is favorable for 2e-WOR from the DFT calculations in Supplementary Fig. 3. In addition to the TEM analysis, the Grazing-incidence X-ray diffraction (GIXRD) measurement in Fig. 4d shows that the formed crystalline particles on FTO have the $LaAlO_3$ perovskite structure (ICDD 01–083–4238), for which the peak at 11.46 ° corresponds to the (100) plane. The 15.7° peak is overlapped by the (110) peak of $LaAlO_3$ and the FTO substrate peak; however, the HRTEM confirms the (110) facet for $LaAlO_3$. Since the GIXRD was collected with the X-rays with its incident energy of 17.0 keV and wavelength of 0.729 Å[60], the two theta values are different from those with the general Cu Kα (1.54 Å). All the above results confirm that the crystal structure of $LaAlO_3$ is cubic perovskite.

In addition, X-ray photoelectron spectroscopy (XPS) was performed to investigate the surface elemental components of the as-synthesized $LaAlO_3$. The XPS survey profile in Fig. 4e shows that the elemental ratio between La and Al was approximately 1. The high-resolution XPS spectra in Fig. 4f show that the La *3d* core level splits into $3d_{3/2}$ and $3d_{5/2}$ components due to the spin-orbit coupling. The observed La $3d_{5/2}$ doublet has a splitting of ~4.0 eV, which agrees with the formation of lanthanum oxide[61,62]. In comparison, the sol-gel synthesized $LaAlO_3$ has a *La* $3d_{5/2}$ doublet of about 3.7 eV, which indicates lanthanum hydroxide species (Supplementary Fig. 13). Furthermore, the O 1 s core level for combustion-synthesized $LaAlO_3$ in Fig. 4h consists of three peaks: La–O, La–O–Al, and Al–O at 529 eV, 530.1 eV, and 531.2 eV, respectively[63–65]. In another way, the deconvoluted O *1s* peak also contains a slight amount of oxygen vacancies in the lattice and the ratio between the oxide and oxygen vacancy is approximately 10:1 based on their integrated areas, which can contribute to the conductivity of $LaAlO_3$ (Supplementary Fig. 14). The O *1 s* peaks for sol-gel synthesized $LaAlO_3$ imply that the surface contains the hydroxide species rather than the oxides (Supplementary Fig. 13). Those analyses indicate that the solution-based combustion reaction effectively converts the metal precursors into crystalline perovskite oxide[58,66].

Evaluation of electrocatalytic H_2O_2 evolution properties on $LaAlO_3$ perovskite oxide

Figure 5a plots the linear sweep voltammetry (LSV) curves of the combustion-synthesized $LaAlO_3$ on FTO/glass and the bare FTO/glass in two different electrolytes: 2 M $KHCO_3$ (pH = 8.3) and 4 M K_2CO_3/$KHCO_3$ (molar ration of 1:7, pH = 11). The 2 M $KHCO_3$ is the commonly used electrolyte for 2e-WOR[18,32,49], while the 4 M K_2CO_3/$KHCO_3$ electrolyte was recently identified as a better electrolyte with higher

https://doi.org/10.1038/s41467-022-34884-4

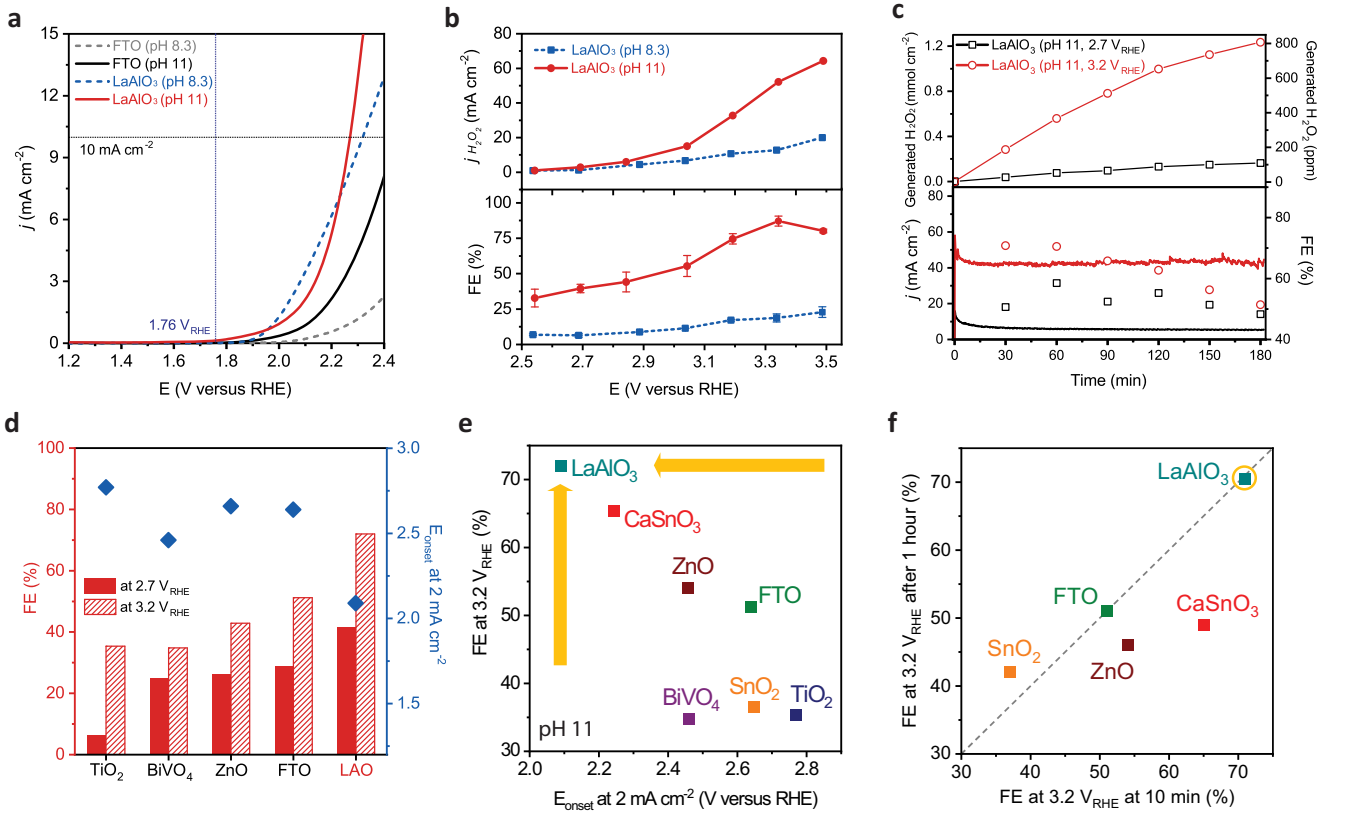

Fig. 5 | Electrochemical performance. a Linear sweep voltammetry curves of $LaAlO_3$ anode compared to FTO/glass substrate in the electrolyte of 2 M $KHCO_3$ (pH 8.3) and 4 M K_2CO_3/$KHCO_3$ (pH 11). All curves are 95 % iR-compensated. **b** The calculated H_2O_2 current density and selectivity of $LaAlO_3$ anode as a function of potential in different electrolytes, and **c** the generated H_2O_2 amount, selectivity, and stability of the $LaAlO_3$ anode at different potentials, 2.7 and 3.2 V vs. RHE for 3 h. **d** Comparison of Faradaic efficiencies at different potentials and onset potentials to reach 2 mA cm^{-2} with the previously reported materials in pH 11. **e** Selectivity vs. activity plot for different metal oxides in the electrolyte of 4 M K_2CO_3/$KHCO_3$ (pH 11) at 3.2 V vs. RHE. **f** Comprehensive plot for selectivity and stability in the electrolyte of 4 M K_2CO_3/$KHCO_3$ (pH 11) at 3.2 V vs. RHE. The *x*-axis is the FE at time $t = 10$ min. The *y*-axis is the FE at time $t = 1$ h. The diagonal dashed line is the expected response for a stable catalyst.

selectivity towards 2e-WOR[33,67]. Indeed, both $LaAlO_3$/FTO and bare FTO exhibit earlier onset potentials in the newly optimized 4 M K_2CO_3/$KHCO_3$ electrolyte. The overpotentials at 10 mA cm^{-2} of $LaAlO_3$/FTO film were measured to be 560 mV in 2 M $KHCO_3$ and 510 mV in 4 M K_2CO_3/$KHCO_3$ (equilibrium potential: 1.76 V vs. RHE). In both electrolytes, the overpotentials of $LaAlO_3$/FTO are smaller than those of bare FTO. The electrochemical impedance spectroscopy (EIS) analysis was conducted to compare the conductivity of $LaAlO_3$ and FTO substrate at 2.7 V vs. RHE (Supplementary Fig. 15). The data were fitted with a REAP2CPE equivalent circuit model in which there were three types of resistances: resistance in the electrolyte solution (R1), charge transfer resistance inside bulk catalyst (R2), and charge transfer resistance at the interface between the catalyst and electrolyte (R3). Here, we could emphasize R2 and R3 values, which contribute to the conductivity inside the bulk of the catalyst material and at the interface between the material surface and the electrolyte. Here, $LaAlO_3$ film shows roughly 3.5 times lower bulk and interface resistances than FTO itself at 2.7 V vs. RHE, which is the desired potential for H_2O_2 production. This presumably results from the oxygen vacancy in the lattice (Supplementary Fig. 14). This can also be evidence that our $LaAlO_3$ is not an insulating material compared to FTO. In addition, we also measured the activity for some stable perovskite oxides, based on the formation energies (Fig. 1), in 4 M K_2CO_3/$KHCO_3$ (pH 11; Supplementary Fig. 16). All perovskite oxides here were synthesized by the same method as that for $LaAlO_3$. We found that $SmCuO_3$ and $GdCuO_3$ also showed relatively good activity (610 and 660 mV at 10 mA cm^{-2}, respectively) but were still inferior to the activity of $LaAlO_3$. Figure 5b shows that the H_2O_2 current densities (j_{H2O2}) and the Faradaic efficiencies (FE) of $LaAlO_3$/FTO are higher in 4 M K_2CO_3/$KHCO_3$ (pH 11) than those in 2 M $KHCO_3$ (pH 8.3), especially at higher bias, and the peak FE reaches 87 % at 3.34 V vs. RHE in the optimized electrolyte vs. 23 % at 3.5 V vs. RHE in 2 M $KHCO_3$ (see Methods section for details). We further tested the stability of $LaAlO_3$/FTO in 4 M K_2CO_3/$KHCO_3$ under two current densities of 3 and 33 mA cm^{-2} at 2.7 and 3.2 V vs. RHE, respectively. Figure 5c shows that the $LaAlO_3$/FTO has a smaller FE decrease at 2.8 V vs. RHE (from 51% to 48%) than at 3.2 V vs. RHE (70% to 51%) after 3 h of the test. After 3 h of the durability test, 0.16 mmol cm^{-2} (128 ppm) and 1.23 mmol cm^{-2} (808 ppm) of H_2O_2 were generated at 2.7 and 3.2 V vs. RHE, respectively, in comparison to only 70 µmol cm^{-2} at 2.7 V vs. RHE for bare FTO (Supplementary Fig. 17). After the stability test, we measured the post-situ XPS and SEM images to assess any elemental composition and morphology changes (Supplementary Figs. 18 and 19). No compositional degradations in La *3d*, Al *2p*, and O *1 s* regions were observed from the post-situ XPS analysis after 3 h of the durability test nor any morphological degradation from the SEM images.

Figure 5d compares the FEs (right) at 2.7 and 3.2 V vs. RHE of $LaAlO_3$/FTO and the onset potential to attain 2 mA cm^{-2} (left) with previously reported metal oxide catalysts on FTO in the same electrolyte (4 M K_2CO_3/$KHCO_3$). The $LaAlO_3$ perovskite oxide exhibits much higher FEs and lower onset potential than TiO_2, $BiVO_4$, ZnO, and FTO. Additionally, $LaAlO_3$ has the lowest overpotential to reach 2 mA cm^{-2} among all the previously reported metal oxides in 2 M $KHCO_3$ in Supplementary Fig. 20. Furthermore, we conducted the activity, stability, and selectivity test for some of the state-of-the-art

metal oxides ($CaSnO_3$, ZnO, and SnO_2) to compare with those for $LaAlO_3$ in 4 M K_2CO_3/$KHCO_3$ (pH 11), showing that $LaAlO_3$ exhibited the lower overpotential, higher FEs and generated H_2O_2 amount (Supplementary Fig. 21). Other oxides ($BiVO_4$, TiO_2, ZnO, and FTO) were investigated for electrochemical H_2O_2 production under the same condition in our previous study[32,67]. In Supplementary Fig. 22 (Reprinted (adapted) with permission from ref. 68. Copyright 2021 American Chemical Society.)[68], the production rate of H_2O_2 for $LaAlO_3$ is much higher than other reported metal oxides and similar to the boron-doped diamond (BDD). Finally, we assessed different state-of-the-art metal oxides by plotting FEs at 3.2 V_{RHE} vs. onset potential to reach 2 mA cm^{-2} in 4 M K_2CO_3/$KHCO_3$ (pH 11) in Fig. 5e. $LaAlO_3$ is positioned at the very upper left side of the plot, which means the most active and selective catalyst among different metal oxides. Figure 5f also demonstrates the comprehensive plot for the selectivity and stability in 4 M K_2CO_3/$KHCO_3$ (pH 11) at 3.2 V vs. RHE. The *x*-axis is the FE at $t = 10$ min, and the *y*-axis is the FE at $t = 1$ h. The diagonal dashed line is the expected response for a stable catalyst. $LaAlO_3$ is located on both the expected response line and the highest FE region, which indicates the most selective and stable catalyst among the known state-of-the-art metal oxides. These results indicate that the $LaAlO_3$ catalyst has superior activity and selectivity for 2e-WOR to produce H_2O_2, especially in the recently optimized 4 M K_2CO_3/$KHCO_3$ electrolyte.

Here, we utilized combined computational screening and experimental results to identify $LaAlO_3$ as the most stable, active, and selective catalyst reported thus far for 2e-WOR to H_2O_2 production. First, we extensively investigated a library of more than 2000 perovskites to identify 32 stable perovskites at pH=8 and 10 stable perovskites at pH = 11 for 2e-WOR. Among them, $LaAlO_3$ was found as the most stable with the smallest formation energy under both pH conditions. Then, in order to provide a potential to examine the 2e-WOR activity, we synthesized $LaAlO_3$ via self-sustaining solution-combustion method. The synthesized $LaAlO_3$ exhibits a cubic crystal structure with dominant planes of (100) and (110). The catalytic properties of $LaAlO_3$ towards 2e-WOR were evaluated at two different electrolytes: 2 M $KHCO_3$ (pH 8.3) and 4 M K_2CO_3/$KHCO_3$ (1:7, pH 11), and $LaAlO_3$ shows better activity towards 2e-WOR than TiO_2, $BiVO_4$, ZnO, and FTO in both electrolytes. $LaAlO_3$ achieves a superior 2e-WOR activity (510 mV of the overpotential to reach 10 mA cm^{-2}), excellent selectivity (the peak FE of 87 % at 3.34 V vs. RHE), and stability (only 3 % of the FE degradation after 3 h).

Methods

DFT calculations

Density functional theory (DFT) calculations were performed using the Vienna ab initio Simulation Package (VASP) code[69]. The projector augmented wave (PAW) method was used to describe the interactions between electrons and ion cores[70]. The electron exchange and correlation energy were described using the revised Perdew-Burke-Ernzerhof (RPBE) functional[71]. A plane-wave cutoff energy of 500 eV was utilized to expand the wavefunctions. The total energy convergence was set to be lower than 10^{-6} eV, and the convergence criterion for geometry optimizations was set to a maximum force of 0.02 eV/Å. *U* values of 7.0 and 4.5 eV were set for $LaNiO_3$ and $LaCuO_3$, respectively, to describe the strong correlation effect of Ni *3d* and Cu *3d* by the DFT + U method. Periodic boundary conditions were used in all directions, and the facets of (100), (110), and (111) for $LaAlO_3$ were investigated. A Monkhorst-Pack grid with dimensions of $4 \times 4 \times 1$ was used for sampling the first Brillouin zones[72], and 15 Å of vacuum in the z-direction was employed to separate the slabs.

The two-electron reaction pathway for WOR can be written as:

$$H_2O + * \rightarrow *OH + (H^+ + e^-)$$

$$H_2O + * \rightarrow *OH + (H^+ + e^-)$$

$$*OH + *OH \rightarrow H_2O_2$$

The reaction energy of each elementary step for the WOR has been calculated based on the method developed by Nørskov et al. [73] as follows:

$$\Delta G = \Delta E + \Delta ZPE - T\Delta S + \Delta G_U + \Delta G_{pH} + \Delta G_{field} \quad (1)$$

$$\Delta G_U = eU \quad (2)$$

$$\Delta G_{pH} = 0.0592 \times pH \quad (3)$$

where ΔE is the total energy change obtained from DFT calculations, ΔZPE is the change of zero-point energy, T is the temperature (298.15 K), and ΔS represents the entropy change. U is the electrode potential (vs. reversible hydrogen electrode), and e^- is the charge transferred. ΔG_{field} is the free energy correction due to the electrochemical double layer and is neglected as suggested in previous studies[73,74]. Zero-point energy and entropies of the adsorbed species were calculated from the vibrational frequencies (Supplementary Table 3). We used the computational hydrogen electrode model, which exploits $G(H^+ + e^-) = \frac{1}{2}G(H_2)$ under $pH = 0$ and $U = 0$ V. The free energy of H_2O was calculated from gas-phase H_2O at 0.035 bar, 298.15 K.

To study the stabilities of (100), (110), and (111) facets for $LaAlO_3$, we calculated their surface energies using the following equation:

$$\Upsilon = (E_{tot} - N_{La}{}^*E_{bulk})/\mathrm{N} \quad (4)$$

where E_{tot} and E_{bulk}. refer to the total energies of the structures with a specific facet and unit bulk, N_{La} and N refers to the numbers of Lanthanum and total atoms, respectively.

Computational screening

A large library of more than 2000 perovskites has been investigated using high-throughput screening. In the first step, we set the stability criteria to E above hull ≤ 0.1 eV to filter the stable perovskites. Next, we used the Pourbaix diagram to predict the compositions of oxides and identify the electrochemical stability of perovskites under different reaction conditions (various pH and potentials). Pourbaix diagram was constructed by using Python Material Genome (Pymatgen)[48] and Materials Project[40].

Sample preparation

All chemical precursors were purchased from Sigma Aldrich. We deployed the acetylacetone-based sol-gel combustion synthesis. First, 0.2 M of $La(NO_3)_3{\cdot}6H_2O$ and $Al(NO_3)_3{\cdot}9H_2O$ were dissolved in 5 ml of 2-methoxyethanol in a 1:1 ratio, followed by 0.2 ml of acetylacetone. After completely dissolving the metal salts, 114 µl of NH_4OH was added to the solution. Then, the solution was aged for 12 h. Next, the 80 µl of the precursor solution was spin-coated on the cleaned fluorine-doped tin oxide (FTO, 7–8 ohm/sq, MSE supplies) substrate at 3000 rpm for 20 s, then annealed at 300 °C for 30 min under air. Here, a combustion-based synthetic approach is applied to oxide thin films, using acetylacetone as a 'fuel' and metal nitrates as oxidizers[58].

Materials characterizations

Sample morphology was investigated using scanning electron microscopy (SEM, FEI Magellan 400), and high-resolution, dark-field, and energy-dispersive X-ray spectroscopy (EDS) mapping images were collected by transmission electron microscopy (TEM, FEI Tecnai G2 F20 X-TWIN, 200 kV) at Stanford Nano Shared Facilities (SNSF). The TEM instrument was run using the TIA interface, and Gatan Digital

Micrograph was employed to calculate the material d-spacing value with a Fast Fourier Transform (FFT) image. Here, d-spacing was determined by the gap between two symmetrical diffraction points in the FFT image.

Grazing-incidence X-ray diffraction (GIXRD) was measured at Beamline 2-1 of the Stanford Synchrotron Radiation Lightsource at SLAC National Accelerator Laboratory with an incident energy of 17.0 keV (0.729 Å) and a Huber 2-circle goniometer. The beam was sliced down to a vertical height of ~ 30 µm and a nominal width of 1 mm. The scattered X-rays were determined using a Pilatus 100 K area detector from Dectris with 487 × 195 pixels (172 µm × 172 µm pixel size). During measurements, the incident angle of the X-ray remained fixed while the detector was moved through a range of diffraction angles.

The surface analysis with an elemental quantification was investigated using X-ray photoelectron spectroscopy (XPS, PHI VersaProbe 3) that uses a monochromatized Al Kα radiation (1486 eV). All XPS spectra were calibrated to the C 1 s peak at a binding energy of 284.8 eV. CasaXPS software was used to carry out peak fitting with Shirley backgrounds.

Thermogravimetric and differential scanning calorimetry (TGA/DSC, Setaram Labsys Evo) were simultaneously used to obtain the heat flow and mass change on the precursor solution with the temperature range from 25 to 800 °C at a heating rate of 10 °C/min.

Electrochemical measurement

Electrochemical measurement was conducted using a potentiostat (Model Interface 1010, Gamry) and three-electrode electrochemical cell including $LaAlO_3$/FTO working electrode (geometric area of 0.502 cm^2), carbon rod counter electrode[75,76], and Ag/AgCl (KCl Sat.) reference electrode in the 30 mL of the electrolyte of 2 M $KHCO_3$ (pH 8.3) and 4 M K_2CO_3/$KHCO_3$ (1:7, pH 11). The measured potentials versus Ag/AgCl were converted to the potentials versus reversible hydrogen electrode (RHE) by the equation below:

$$E_{RHE} = E_{Ag/AgCl} + 0.059 \times pH + 0.197 \quad (5)$$

The electrochemical activity was evaluated using linear sweep voltammetry (LSV), sweeping from 1.2 V to 2.4 V vs. RHE at a scan rate of 50 mV/s. All curves are 95% iR-compensated. The EIS measurement was conducted between 20 kHz and 0.05 kHz at 2.7 V vs. RHE for all samples. Chronoamperometry assessed stability, applying a constant potential of 2.7 and 3.2 V vs. RHE for 3 h. H_2O_2 was collected during the chronoamperometry test at different times, followed by UV-vis absorbance measurement of the mixture solution of cobalt sulfate and the electrolyte, including the produced hydrogen peroxide. Before measuring the absorbance, the complexation time is required for 30 min. A calibration curve was measured with the same procedure but using commercial hydrogen peroxide [9]. H_2O_2 with higher concentration was quantified using the titration method with potassium permanganate and sulfuric acid, based on the following reaction:

$$2MnO_4^-(aq) + 6H^+(aq) + 5H_2O_2(aq) \rightarrow 2Mn^{2+}(aq) + 8H_2O(l) + 5O_2(g)$$

Selectivity was evaluated by the calculation of Faradaic efficiency, which is determined by the equation below:

$$FE = \frac{n \times N_{H_2O_2} \times F}{I \times t} \quad (6)$$

where n, N_{H2O2}, F, I, and t represent the number of electrons, the mole of H_2O_2 produced, faradaic constant, measured current, and time, respectively. The FEs at each potential were calculated by applying the absorbance measurement from its calibration curve (Supplementary Fig. 23) after the chronoamperometry test for 10 min, as shown in the Methods section. The inset picture in Supplementary Fig. 23 indicates the mixture of cobalt sulfate dye and the electrolyte, including the generated H_2O_2: the more greenish the solution looks, the more H_2O_2 is generated.

Data availability

The data that support the plots within this paper and other findings of this study are available from the corresponding authors on reasonable request.

References

1. Kern, W. *Handbook Of Semiconductor Wafer Cleaning Technology* (Noyes Publication, 1993).
2. Broadway, D. A. et al. Spatial mapping of band bending in semiconductor devices using in situ quantum sensors. *Nat. Electron.* **1**, 502–507 (2018).
3. Tanev, P. T., Chibwe, M. & Pinnavaia, T. J. Titanium-containing mesoporous molecular sieves for catalytic oxidation of aromatic compounds. *Nature* **368**, 321–323 (1994).
4. Lane, B. S. & Burgess, K. Metal-catalyzed epoxidations of alkenes with hydrogen peroxide. *Chem. Rev.* **103**, 2457–2474 (2003).
5. Lin, Y. J. et al. Thermocatalytic hydrogen peroxide generation and environmental disinfection by Bi_2Te_3 nanoplates. *Nat. Commun.* **12**, 180 (2021).
6. Campos-Martin, J. M., Blanco-Brieva, G. & Fierro, J. L. G. Hydrogen peroxide synthesis: an outlook beyond the anthraquinone process. *Angew. Chem. Int. Ed.* **45**, 6962–6984 (2006).
7. Siahrostami, S. et al. A review on challenges and successes in atomic-scale design of catalysts for electrochemical synthesis of hydrogen peroxide. *ACS Catal.* **10**, 7495–7511 (2020).
8. Siahrostami, S., Li, G. L., Viswanathan, V. & Nørskov, J. K. One- or two-electron water oxidation, hydroxyl radical, or H_2O_2 evolution. *J. Phys. Chem. Lett.* **8**, 1157–1160 (2017).
9. Fuku, K., Miyase, Y., Miseki, Y., Gunji, T. & Sayama, K. Enhanced oxidative hydrogen peroxide production on conducting glass anodes modified with metal oxides. *ChemistrySelect* **1**, 5721–5726 (2016).
10. Lu, Z. et al. High-efficiency oxygen reduction to hydrogen peroxide catalysed by oxidized carbon materials. *Nat. Catal.* **1**, 156–162 (2018).
11. Chang, Q. et al. Promoting H_2O_2 production via 2-electron oxygen reduction by coordinating partially oxidized Pd with defect carbon. *Nat. Commun.* **11**, 2178 (2020).
12. Yang, S., Kim, J., Tak, Y. J., Soon, A. & Lee, H. Single-atom catalyst of platinum supported on titanium nitride for selective electrochemical reactions. *Angew. Chem. Int. Ed.* **55**, 2058–2062 (2016).
13. Mounfield, W. P., Garg, A., Shao-Horn, Y. & Román-Leshkov, Y. Electrochemical oxygen reduction for the production of hydrogen peroxide. *Chem* **4**, 18–19 (2018).
14. Chen, S. et al. Designing boron nitride islands in carbon materials for efficient electrochemical synthesis of hydrogen peroxide. *J. Am. Chem. Soc.* **140**, 7851–7859 (2018).
15. Jiang, K. et al. Highly selective oxygen reduction to hydrogen peroxide on transition metal single atom coordination. *Nat. Commun.* **10**, 3997 (2019).
16. Suk, M., Chung, M. W., Han, M. H., Oh, H. S. & Choi, C. H. Selective H_2O_2 production on surface-oxidized metal-nitrogen-carbon electrocatalysts. *Catal. Today* **359**, 99–105 (2021).
17. Ando, Y. & Tanaka, T. Proposal for a new system for simultaneous production of hydrogen and hydrogen peroxide by water electrolysis. *Int. J. Hydrog. Energy* **29**, 1349–1354 (2004).
18. Shi, X. et al. Understanding activity trends in electrochemical water oxidation to form hydrogen peroxide. *Nat. Commun.* **8**, 701 (2017).

19. Park, S. Y. et al. $CaSnO_3$: an electrocatalyst for two-electron water oxidation reaction to form H_2O_2. *ACS Energy Lett.* **4**, 352–357 (2019).
20. Izgorodin, A., Izgorodina, E. & MacFarlane, D. R. Low overpotential water oxidation to hydrogen peroxide on a MnO_x catalyst. *Energy Environ. Sci.* **5**, 9496 (2012).
21. Kelly, S. R. et al. ZnO as an active and selective catalyst for electrochemical water oxidation to hydrogen peroxide. *ACS Catal.* **9**, 4593–4599 (2019).
22. Kang, T. et al. Efficient hydrogen peroxide (H_2O_2) synthesis by $CaSnO_3$ via two-electron water oxidation reaction. *ACS Sustain. Chem. Eng.* **8**, 15005–15012 (2020).
23. Miyase, Y., Miseki, Y., Gunji, T. & Sayama, K. Efficient H_2O_2 production via H_2O oxidation on an anode modified with Sb-containing mixed metal oxides. *ChemElectroChem* **7**, 2448–2455 (2020).
24. Zhang, C. et al. High yield electrosynthesis of hydrogen peroxide from water using electrospun $CaSnO_3$@carbon fiber membrane catalysts with abundant oxygen vacancy. *Adv. Funct. Mater.* **31**, 2100099 (2021).
25. Baek, J. H. et al. Selective and efficient Gd-doped $BiVO_4$ photoanode for two-electron water oxidation to H_2O_2. *ACS Energy Lett.* **4**, 720–728 (2019).
26. Li, L., Hu, Z. & Yu, J. C. On-demand synthesis of H_2O_2 by water oxidation for sustainable resource production and organic pollutant degradation. *Angew. Chem. Int. Ed.* **59**, 20538–20544 (2020).
27. Fuku, K. et al. Photoelectrochemical hydrogen peroxide production from water on a WO_3/$BiVO_4$ photoanode and from O_2 on an Au cathode without external bias. *Chem. Asian J.* **12**, 1111–1119 (2017).
28. Fuku, K., Miyase, Y., Miseki, Y., Gunji, T. & Sayama, K. WO_3/$BiVO_4$ photoanode coated with mesoporous Al_2O_3 layer for oxidative production of hydrogen peroxide from water with high selectivity. *RSC Adv.* **7**, 47619 (2017).
29. Xia, C. et al. Confined local oxygen gas promotes electrochemical water oxidation to hydrogen peroxide. *Nat. Catal.* **3**, 125–134 (2020).
30. Wenderich, K., Nieuweweme, B. A. M., Mul, G. & Mei, B. T. Selective electrochemical oxidation of H_2O to H_2O_2 using boron-doped diamond: an experimental and techno-economic evaluation. *ACS Sustain. Chem. Eng.* **9**, 7803–7812 (2021).
31. Mavrikis, S., Göltz, M., Rosiwal, S., Wang, L. & Ponce De León, C. Boron-doped diamond electrocatalyst for enhanced anodic H_2O_2 production. *ACS Appl. Energy Mater.* **3**, 3169–3173 (2020).
32. Gill, T. M., Vallez, L. & Zheng, X. The role of bicarbonate-based electrolytes in H_2O_2 production through two-electron water oxidation. *ACS Energy Lett.* **6**, 2854–2862 (2021).
33. Mavrikis, S. et al. Effective Hydrogen Peroxide Production from Electrochemical Water Oxidation. *ACS Energy Lett.* **6**, 2369–2377 (2022).
34. Viswanathan, V., Hansen, H. A. & Nørskov, J. K. Selective electrochemical generation of hydrogen peroxide from water oxidation. *J. Phys. Chem. Lett.* **6**, 4224–4228 (2015).
35. Prakash, A. et al. Wide bandgap $BaSnO_3$ films with room temperature conductivity exceeding 104 S cm^{-1}. *Nat. Commun.* **8**, 15167 (2017).
36. Sun, C., Alonso, J. A. & Bian, J. Recent advances in perovskite-type oxides for energy conversion and storage applications. *Adv. Energy Mater.* **11**, 2000459 (2021).
37. Hwang, J. et al. Perovskites in catalysis and electrocatalysis. *Science* **358**, 751–756 (2017).
38. Pan, Y. et al. Direct evidence of boosted oxygen evolution over perovskite by enhanced lattice oxygen participation. *Nat. Commun.* **11**, 2002 (2020).
39. Peña, M. A. & Fierro, J. L. G. Chemical structures and performance of perovskite oxides. *Chem. Rev.* **101**, 1981–2017 (2001).
40. Jain, A. et al. Commentary: The materials project: a materials genome approach to accelerating materials innovation. *APL Mater.* **1**, 011002 (2013).
41. Persson, K. A., Waldwick, B., Lazic, P. & Ceder, G. Prediction of solid-aqueous equilibria: Scheme to combine first-principles calculations of solids with experimental aqueous states. *Phys. Rev. B Condens. Matter Mater. Phys.* **85**, 235438 (2012).
42. Singh, A. K., Montoya, J. H., Gregoire, J. M. & Persson, K. A. Robust and synthesizable photocatalysts for CO_2 reduction: a data-driven materials discovery. *Nat. Commun.* **10**, 443 (2019).
43. Gunasooriya, G. T. K. K. & Norskov, J. K. Analysis of acid-stable and active oxides for the oxygen evolution reaction. *ACS Energy Lett.* **5**, 3778–3787 (2020).
44. Man, I. C. et al. Universality in oxygen evolution electrocatalysis on oxide surfaces. *ChemCatChem* **3**, 1159–1165 (2011).
45. Montoya, J. H., Doyle, A. D., Nørskov, J. K. & Vojvodic, A. Trends in adsorption of electrocatalytic water splitting intermediates on cubic ABO_3 oxides. *Phys. Chem. Chem. Phys.* **20**, 3813–3818 (2018).
46. Shi, X., Back, S., Gill, T. M., Siahrostami, S. & Zheng, X. Electrochemical synthesis of H_2O_2 by two-electron water oxidation reaction. *Chem* **7**, 38–63 (2021).
47. Singh, A. K. et al. Electrochemical stability of metastable materials. *Chem. Mater.* **29**, 10159–10167 (2017).
48. Ong, S. P. et al. Python materials genomics (pymatgen): a robust, open-source python library for materials analysis. *Comput. Mater. Sci.* **68**, 314–319 (2013).
49. Fuku, K. & Sayama, K. Efficient oxidative hydrogen peroxide production and accumulation in photoelectrochemical water splitting using a tungsten trioxide/bismuth vanadate photoanode. *Chem. Commun.* **52**, 5406–5409 (2016).
50. Fan, L. et al. CO_2/carbonate-mediated electrochemical water oxidation to hydrogen peroxide. *Nat. Commun.* **13**, 2668 (2022).
51. Kusama, H., Kodera, M., Yamashita, K. & Sayama, K. Insights into the carbonate effect on water oxidation over metal oxide photocatalysts/photoanodes. *Phys. Chem. Chem. Phys.* **24**, 5894–5902 (2022).
52. Zvereva, I., Smirnov, Y., Gusarov, V., Popova, V. & Choisnet, J. Complex aluminates $RE_2SrAl_2O_7$ (RE = La, Nd, Sm-Ho): cation ordering and stability of the double perovskite slab-rocksalt layer P_2/RS intergrowth. *Solid State Sci.* **5**, 343–349 (2003).
53. Jancar, B., Suvorov, D., Valant, M. & Drazic, G. Characterization of $CaTiO_3$-$NdAlO_3$ dielectric ceramics. *J. Eur. Ceram. Soc.* **23**, 1391–1400 (2003).
54. Vidyasagar, K., Gopalakrishnan, J. & Rao, C. N. R. Synthesis of complex metal oxides using hydroxide, cyanide, and nitrate solid solution precursors. *J. Solid State Chem.* **58**, 29–37 (1985).
55. Lux, B. C., Clark, R. D., Salazar, A., Sveum, L. K. & Krebs, M. A. Aerosol generation of lanthanum aluminate. *J. Am. Ceram. Soc.* **76**, 2669–2672 (1993).
56. Shoup, S. S., Paranthaman, M., Beach, D. B., Specht, E. D. & Williams, R. K. Sol-gel synthesis of $LaAlO_3$; epitaxial growth of $LaAlO_3$ thin films on $SrTiO_3$ (100). *J. Mater. Res.* **12**, 1017–1021 (1997).
57. Da Silva, C. A. & De Miranda, P. E. V. Synthesis of $LaAlO_3$ based materials for potential use as methane-fueled solid oxide fuel cell anodes. *Int. J. Hydrog. Energy* **40**, 10002–10015 (2015).
58. Kim, M. G., Kanatzidis, M. G., Facchetti, A. & Marks, T. J. Low-temperature fabrication of high-performance metal oxide thin-film electronics via combustion processing. *Nat. Mater.* **10**, 382–388 (2011).
59. Epifani, M., Melissano, E., Pace, G. & Schioppa, M. Precursors for the combustion synthesis of metal oxides from the sol–gel processing of metal complexes. *J. Eur. Ceram. Soc.* **27**, 115–123 (2007).
60. Landers, A. T. et al. A refraction correction for buried interfaces applied to in situ grazing-incidence X-ray diffraction studies on Pd electrodes. *J. Synchrotron Radiat.* **28**, 919–923 (2021).
61. Li, J. P. H. et al. Understanding of binding energy calibration in XPS of lanthanum oxide by: In situ treatment. *Phys. Chem. Chem. Phys.* **21**, 22351–22358 (2019).

62. Sunding, M. F. et al. XPS characterisation of in situ treated lanthanum oxide and hydroxide using tailored charge referencing and peak fitting procedures. *J. Electron Spectrosc. Relat. Phenomena* **184**, 399–409 (2011).
63. Zhao, L., Liu, H., Wang, X., Feng, X. & Fei, C. Band alignments of O_3-based and H_2O-based amorphous $LaAlO_3$ films on silicon by atomic layer deposition. *J. Mater. Sci. Mater. Electron.* **28**, 803–807 (2017).
64. Ali, K., Choi, K. H., Jo, J. & Lee, Y. W. High rate roll-to-roll atmospheric atomic layer deposition of Al_2O_3 thin films towards gas diffusion barriers on polymers. *Mater. Lett.* **136**, 90–94 (2014).
65. Kim, H. et al. The effects of annealing ambient on the characteristics of La_2O_3 films deposited by RPALD. *J. Electrochem. Soc.* **157**, 479–482 (2010).
66. Ianoş, R., Lazău, R., Borcănescu, S., & Băbuèă, R. Single-step combustion synthesis of $LaAlO_3$ powders and their sintering behavior. *Ceram. Int.* **40**, 7561–7565 (2014).
67. Gill, T. M., Vallez, L. & Zheng, X. Enhancing electrochemical water oxidation toward H_2O_2 via carbonaceous electrolyte engineering. *ACS Appl. Energy Mater.* **4**, 12429–12435 (2021).
68. Mavrikis, S., Perry, S. C., Leung, P. K., Wang, L. & Ponce De León, C. Recent Advances in Electrochemical Water Oxidation to Produce Hydrogen Peroxide: A Mechanistic Perspective. *ACS Sustain. Chem. Eng.* **9**, 76–91 (2021).
69. Kresse, G. & Furthmüller, J. Efficient iterative schemes for ab initio total-energy calculations using a plane-wave basis set. *Phys. Rev. B Condens. Matter Mater. Phys.* **54**, 11169 (1996).
70. Mortensen, J. J., Hansen, L. B. & Jacobsen, K. W. Real-space grid implementation of the projector augmented wave method. *Phys. Rev. B Condens. Matter Mater. Phys.* **71**, 035109 (2005).
71. Hammer, B., Hansen, L. B. & Nørskov, J. K. Improved adsorption energetics within density-functional theory using revised Perdew-Burke-Ernzerhof functionals. *Phys. Rev. B Condens. Matter Mater. Phys.* **59**, 7413 (1999).
72. Monkhorst, H. J. & Pack, J. D. Special points for Brillouin-zone integrations. *Phys. Rev. B* **13**, 5188 (1976).
73. Nørskov, J. K. et al. Origin of the overpotential for oxygen reduction at a fuel-cell cathode. *J. Phys. Chem. B* **108**, 17886–17892 (2004).
74. Kattel, S., Atanassov, P. & Kiefer, B. Stability, electronic and magnetic properties of in-plane defects in graphene: a first-principles study. *J. Phys. Chem. C.* **116**, 8161–8166 (2012).
75. Möller, S. et al. Online monitoring of electrochemical carbon corrosion in alkaline electrolytes by differential electrochemical mass spectrometry. *Angew. Chem. Int. Ed.* **59**, 1585–1589 (2020).
76. Benck, J. D., Pinaud, B. A., Gorlin, Y. & Jaramillo, T. F. Substrate selection for fundamental studies of electrocatalysts and photoelectrodes: Inert potential windows in acidic, neutral, and basic electrolyte. *PLoS ONE* **9**, e107942 (2014).

Acknowledgements

X.Z. would like to thank the National Science Foundation EFRI-DCheM program (Agreement Number: SUB0000425), Stanford Natural Gas Initiative, and Stanford Woods Institute for the Environment for their generous support. J.B. acknowledges Chevron Fellowship in Energy. Part of this work was performed at the Stanford Nano Shared Facilities (SNSF)/Stanford Nanofabrication Facility (SNF), supported by the National Science Foundation under award ECCS–2026822. S.S. and Q.J. acknowledge the support from the University of Calgary's Canada First Research Excellence Fund Program, the Global Research Initiative in Sustainable Low Carbon Unconventional Resources. This research was enabled in part by support provided by computational resource at the University of Calgary (www.rcs.ucalgary.ca) and Compute Canada (www.computecanada.ca).

Author contributions

J.B., Q.J., S.S., and X.Z. conceived the ideas and designed the project. S.S. and X.Z. supervised this project. J. B. carried out the experiments including material synthesis, characterizations, and electrochemical measurements. Q.J. conducted the computational investigations. N.S.J. and A.M. contributed to the material characterization (GIXRD). Y.J. and R.N. contributed to the material characterizations (SEM and TEM). J.B. and Q.J. wrote the draft. J.B., Q.J., S.S. and X.Z. edited the manuscript and finalized. All authors participated in the discussion and editing.

Competing interests

The authors declare no competing interests.

Additional information

Supplementary information The online version contains supplementary material available at https://doi.org/10.1038/s41467-022-34884-4.

Correspondence and requests for materials should be addressed to Samira Siahrostami or Xiaolin Zheng.

Peer review information *Nature Communications* thanks the other anonymous reviewer(s) for their contribution to the peer review of this work.